


Direct imaging of the hyperfine depolarization in electronically excited NO molecules

Dai Ikeda ¹, Kenta Mizuse ^{1,2,*}, and Yasuhiro Ohshima ^{1,†}

¹Department of Chemistry, School of Science, Tokyo Institute of Technology, 2-12-1-W4-9, Ookayama, Meguro-ku, Tokyo 152-8550, Japan

²Department of Chemistry, School of Science, Kitasato University 1-15-1-S403, Kitasato, Minami-ku, Sagami-hara, Kanagawa 252-0373, Japan

 (Received 21 December 2022; revised 30 March 2023; accepted 31 March 2023; published 17 April 2023)

We visualize the hyperfine depolarization dynamics of electronically excited nitric oxide (NO) molecules. Pump-probe ion-imaging measurements have been performed to track the spatiotemporal propagation of the angular distribution of NO ($A^2\Sigma^+$, $v = 0$, $J = 3/2$, $N = 2$), excited by ultraviolet nanosecond laser pump pulses resonant with the $R_{21}(1/2)$ transition. Femtosecond intense probe pulses induced Coulomb explosion of the excited NO molecules, where fragment N^+ and O^+ ions were ejected along the direction of the molecular axis just before the explosion. The space-slice imaging coupled with the circularly polarized probe pulse, recently developed in this research group [K. Mizuse *et al.*, *Rev. Sci. Instrum.* **90**, 103107 (2019)] has directly (i.e., without any mathematical reconstruction procedure) provided the two-dimensional section of the molecular-axis distribution, which clearly shows evolution in the nanosecond regime. We have developed a model to reproduce the experimentally captured images by considering a time-dependent density matrix for the excitation of multiple hyperfine states. The model has been proven to be fully compatible with the spherical-tensor-operator formalism [A. J. Orr-Ewing and R. N. Zare, *Annu. Rev. Phys. Chem.* **45**, 315 (1994)], and the initially prepared density matrices have been retrieved successfully from the analysis of time-dependent molecular-axis distribution.

DOI: [10.1103/PhysRevA.107.043116](https://doi.org/10.1103/PhysRevA.107.043116)

I. INTRODUCTION

Angular momentum vectors pertinent to spatial distribution of electrons or molecular frameworks are often modulated and/or decayed by the interaction with other angular momenta or an external environment. This effect is commonly termed “angular momentum depolarization (AMD)” [1–3]. The earliest investigations based on (zero-field) quantum-beat spectroscopy date back almost a half century [4–9]. Oscillation of emission intensity in an atomic system was observed, and this experimental finding was attributed to the interference between coherently excited fine [4–7] or hyperfine [8,9] eigenstates, as reviewed by Hack and Huber [10]. Fano and Macek developed a theoretical framework to treat AMD [1]: here the precession of the electronic orbital angular momentum, initially prepared in an anisotropic manner, was interpreted with respect to the coupling with electronic and/or nuclear spins. To explore hyperfine structure, hyperfine quantum-beat spectroscopy has been applied also to the molecular systems [11,12]. Since then, there have been a number of reports on AMD pertinent to molecular rotation, based on polarized laser spectroscopy [13], angle-resolved photoelectron spectroscopy [14], and time-of-flight mass spectrometry with photodissociation [15–17]. Along with the experimental studies, there have been some theoretical considerations devoted to AMD [2,3,18,19]. Especially, a spherical-tensor-operator formalism by Orr-Ewing

and Zare [2,3] has been applied to reproduce the experimentally observed time-modulated signals with appropriate parametrization.

Polarization of molecular rotational angular momenta leads to spatially aligned or antialigned distribution pertinent to the molecular axes. Thus, controlling rotational angular momenta has been extensively explored by various methods [20–23] and comes to play an essential role in recent advanced experiments utilizing anisotropic molecular ensembles, e.g., ultrafast x-ray and electron diffraction [24,25], scattering with surface and particle [26,27], and molecular-frame photoelectron spectroscopy [28,29]. Detailed information on molecular orientational distribution can be captured by charged particle imaging [30,31], which has been proven as a versatile tool for investigating photodissociation [32,33] and real-time probing of photoexcited reactions [34,35]. In particular, by incorporating laser-induced Coulomb explosion, ion imaging has been extensively used to visualize rotational dynamics induced by ultrashort intense laser pulses [36–41]. On the contrary, imaging investigation of the depolarization dynamics has been limited so far. In the velocity map imaging (VMI) investigation of the photodissociation of excited hydrogen sulfide radicals, it has been shown that anisotropy of the products is depolarized during the long lifetime in the predissociating excited state [42]. The VMI study on the vibrationally mediated photodissociation of hydrogen chloride has identified time-modulated distribution of the products and the spherical-tensor-operator formalism has been adopted to derive the depolarization coefficients [43]. Quite recently, the Coulomb explosion imaging (CEI) study on the rotational wave packet in I_2 molecules has shown that the hyperfine coupling due to

*mizuse@kitasato-u.ac.jp

†ohshima@chem.titech.ac.jp

the electric quadrupole moment of the iodine nuclei slightly affects the wave-packet propagation at the long-time delay [44]. A theoretical investigation has also shown that the spin-spin and spin-rotation couplings in O_2 also affect its molecular alignment at the long delay [45].

Although the ultimate advantage of the ion imaging is its capability for directly providing the spatial distributions pertinent to the molecular orientation and alignment, we have to remember that experimentally captured images are often biased with anisotropic efficiency in the probing (e.g., ionization) process, as in the cases of the above-mentioned previous studies [42–44]. Recently, the present research group has developed an imaging apparatus with a mechanical slit, which slices three dimensionally expanding ion clouds into two-dimensional (2D) sheets [46,47]. The resultant ion sheets are further repelled in the perpendicular direction by applying a pulsed high voltage to be projected onto a 2D position sensitive detector (PSD). This experimental configuration allows us to take 2D ion images perpendicular to the laser propagation direction. With the combination of the circularly polarized probing laser pulse, the isotropic probing of the pump-pulse-induced dynamics can be realized. Its utility has been demonstrated in the CEI measurements of unidirectionally rotating (UDR) ensembles of nitrogen molecules. Here, the molecular-axis angular distribution has been directly (i.e., without any numerical reconstruction procedure such as Abel inversion) recorded successively for changing pump-probe delays, to provide a “molecular movie” of the UDR wave packet (more properly, the square of its absolute value) [39,46,48,49].

In the present study, we visualize the molecular-axis angular distribution in the electronically excited nitric oxide (NO) molecules, modulated temporally by the hyperfine depolarization. Nitric oxide has been extensively studied as a spectroscopic benchmark, because it is a stable open-shell diatomic molecule exhibiting interesting coupling between several different kinds of angular momenta [50–59]. The hyperfine splitting (hfs) in the first electronically excited state ($A^2\Sigma^+$) has been repeatedly investigated by a variety of experimental approaches, including Stark quantum-beat spectroscopy (in the $v = 0$ vibrational level) [50], hyperfine quantum-beat spectroscopy (at $v = 0$) [51], high-resolution two-photon spectroscopy (at $v = 1$) [52], and optical radio frequency double-resonance spectroscopy (at $v = 3$) [53]. The observed transition frequencies and the determined hfs parameters have been summarized by Brouard and co-workers [51]. Microwave spectroscopy was adopted to determine precise hfs constants in the $X^2\Pi$ electronic ground states [54]. State-selective lifetime measurements [55] and fine (and partially hyperfine) structure resolved spectroscopy [56] have been also reported for the $A^2\Sigma^+$ state. CEI was utilized to visualize the singly occupied molecular orbital of NO in the $X^2\Pi$ and $A^2\Sigma^+$ states [57,58]. Creation of the wave packets composed of the Λ -type doubling states in $X^2\Pi$ was considered by numerical calculation [59].

Recently, we reported the results on the imaging of the rotational wave functions in the electronically excited NO molecules [60]. Since the ^{14}N nucleus possesses nonzero spin ($I = 1$), the molecular rotation should be affected by the hyperfine depolarization, as has been shown in the previous photoelectron study [14], but such an effect was not

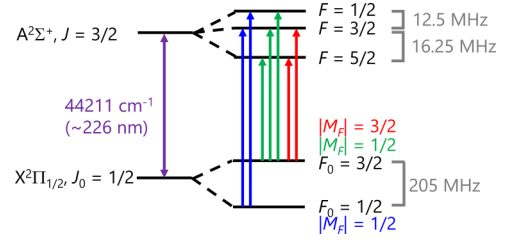


FIG. 1. Energy diagram for the $A^2\Sigma^+ - X^2\Pi^{1/2} R_{21}(1/2)$ transition of NO, including hyperfine splitting in each rotational level.

examined in the previous report [60]. Here, we track the hyperfine depolarization dynamics on the molecular rotation by implementing the CEI coupled with the nanosecond (ns) laser excitation. The linearly polarized ns pulse was set in resonance with the $A^2\Sigma^+ - X^2\Pi_{1/2} R_{21}(1/2)$ transition of NO, to create initial alignment of excited molecules. Then, pump-probe imaging captured the variation of the molecular-axis angular distribution. We also theoretically consider the time-dependent probability distribution pertinent to the wave packets constituting multiple hyperfine eigenstates and compare them with the experimental results. We also demonstrate that these results agree with the formulation deliberated by Orr-Ewing and Zare [2,3].

II. THEORY

In the present study, multiple eigenstates split by the hyperfine interaction in a single rotational level are coherently coupled to create a wave packet of hfs states in the electronically excited NO molecules, the time evolution of which is the issue to be discussed. Since multiple hfs states are populated as the initial states, an incoherent summation of the wave packets has to be considered. Then, we construct the density matrix of the system in the electronically excited state by evaluating the matrix elements from the transition amplitudes. The density matrix will be implemented to give the angular distribution. The density matrix representation is further transformed into the spherical-tensor representation to assess the formulation developed in the previous studies [2,3] and to compare with the experimental results.

A. Wave packets, the density matrix, and the angular distribution

Figure 1 schematically represents the energy levels in the $A^2\Sigma^+ - X^2\Pi_{1/2}$ electronic transition of nitric oxide, which are relevant to the present study. The NO molecule in the $A^2\Sigma^+$ state is appropriately described by Hund’s case ($b_{\beta J}$) [55]. Thus, the hfs eigenstate of NO ($A^2\Sigma^+$) is represented as $|A^2\Sigma^+, N\Lambda S J I M_F\rangle$ (see Appendix A). The angular momenta appearing here are as follows: molecular rotation, \mathbf{R} ; the projection of the electronic orbital angular momentum onto the molecular axis, Λ ; the total angular momentum excluding the spins, $\mathbf{N}(=\mathbf{R} + \Lambda)$; the electronic spin, \mathbf{S} ; the total angular momentum without nuclear spin, $\mathbf{J}(=\mathbf{N} + \mathbf{S})$; the ^{14}N nuclear spin, \mathbf{I} ; and the total angular momentum, $\mathbf{F}(=\mathbf{J} + \mathbf{I})$, with its projection onto the space-fixed Z axis as M_F . Since the magnitude of the fine and hyperfine splitting is

well below a few hundred MHz [51], the hfs has not been fully resolved, even when Doppler-free two-photon spectroscopy was adopted by using single-mode cw lasers [52,56].

In the present study, a conventional ns pulsed laser was used for the electronic excitation of NO molecules. Its pulse duration was ~ 10 ns and the corresponding coherent frequency bandwidth was ~ 100 MHz, which is large enough to simultaneously excite multiple hfs eigenstates to create their coherent superposition, i.e., a wave packet. The actual frequency bandwidth was much larger (reaching to ~ 1 GHz), since the laser operated in multilongitudinal modes. Still, it was narrow enough to selectively excite a single rotational line in the $A^2\Sigma^+ - X^2\Pi^{1/2}$ transition, $R_{21}(1/2)$ in the present case. To summarize, wave packets constituting the hfs eigenstates with $F = 1/2, 3/2$, and $5/2$ in the single fine-structure level with $(N, J, M_J) = (2, 3/2, \pm 1/2)$ should be considered in the present condition. The initial rotational level ($X^2\Pi^{1/2}$, $\bar{\Omega} = 1/2$, $J = 1/2$, with parity $\varepsilon = -1$) has also quite small hfs (~ 200 MHz) [54], and the two hfs eigenstates with $F = 1/2$ and $3/2$ were almost equally populated even in the adiabatically cooled condition (with effective rotational temperature of ~ 2 K). Thus there are six initial states: $|F, M_F\rangle = |1/2, \pm 1/2\rangle$, $|3/2, \pm 1/2\rangle$, and $|3/2, \pm 3/2\rangle$. The accessible excited hfs eigenstates from a certain initial hfs state are restricted by the selection rules for the one-photon transition with linearly polarized light, i.e., $\Delta F = 0, \pm 1$, and $\Delta M_F = 0$, as shown in Fig. 1.

The wave packet created from an initial hfs eigenstate, $|F_0, M_F\rangle$, in the electronic ground state is represented as

$$|\Psi^{(F_0, M_F)}(t)\rangle = \sum_{F_1} C_{F_1}^{(F_0, M_F)} |A^2\Sigma^+, N_1 \Lambda_1 S J_1 I F_1 M_F\rangle e^{-i\omega_{F_1} t}, \quad (1)$$

where subscripts 0 or 1 for each quantum number indicate the electronically ground or excited states, respectively, and ω_F is the angular frequency with $\omega_F/2\pi = 28.75, 12.5$, and 0 MHz for $F = 1/2, 3/2$, and $5/2$, respectively [51]. The summation over F_1 ranges from $|F_0 - 1|$ to $F_0 + 1$. The coefficient $C_{F_1}^{(F_0, M_F)}$ is proportional to the transition probability as

$$\begin{aligned} C_{F_1}^{(F_0, M_F)} &= \frac{\langle A^2\Sigma^+, N_1 \Lambda_1 S J_1 I F_1 M_F | \hat{H}' | X^2\Pi, S\Sigma \bar{\Omega} J_0 I F_0 M_F \varepsilon \rangle}{\hbar\omega_{F_1} - \hbar\omega_{F_0}} \\ &= A \sqrt{(2F_0 + 1)(2F_1 + 1)} (-1)^{F_0 + F_1 - M_F - S} \\ &\quad \times \begin{Bmatrix} J_1 & F_1 & I \\ F_0 & J_0 & 1 \end{Bmatrix} \begin{pmatrix} F_1 & 1 & F_0 \\ -M_F & 0 & M_F \end{pmatrix}, \quad (2) \end{aligned}$$

where $|X^2\Pi, S\Sigma \bar{\Omega} J_0 I F_0 M_F \varepsilon\rangle$ is the parity-adopted eigenfunction in NO ($X^2\Pi$), described in case (a $_{\beta}$) [61]. The light-matter interaction $\hat{H}' = \hat{\mu} \cdot \hat{E}$ is due to the electric dipole moment of the molecule. The coefficient A is independent from F_0, F_1 , and M_F , while it depends on other quantum

numbers, as shown in Appendix B. The brackets $\begin{pmatrix} \cdot & \cdot & \cdot \\ \cdot & \cdot & \cdot \end{pmatrix}$ and $\begin{Bmatrix} \cdot & \cdot & \cdot \\ \cdot & \cdot & \cdot \end{Bmatrix}$ are the Wigner's 3- j and 6- j symbols, respectively.

The density matrix for a single wave packet from the initial hfs eigenstate of $|F_0, M_F\rangle$ is represented as

$$\hat{\rho}^{(F_0, M_F)}(J) = |\Psi^{(F_0, M_F)}\rangle \langle \Psi^{(F_0, M_F)}|. \quad (3)$$

Here J is explicitly specified since it is preserved. Generally, the density matrix element in the coupled representation should have four subscripts as $\rho_{F_1, M_{F_1}, F_2, M_{F_2}}$. However, with the selection rule of excitation by a linearly polarized light, the following relation should be held: $M_{F_1} = M_{F_2} = M_F$. Thus, its matrix elements in the $|F, M_F\rangle$ space in the electronic excited state are given as

$$\begin{aligned} \rho_{F_1, F_2}^{(F_0, M_F)}(J, t) &\equiv \langle F_1 M_F | \hat{\rho}^{(F_0, M_F)}(J, t) | F_2 M_F \rangle \\ &= \rho_{F_1, F_2}^{(F_0, M_F)}(J, t = 0) e^{-i(\omega_{F_1} - \omega_{F_2})t}, \quad (4) \end{aligned}$$

with

$$\rho_{F_1, F_2}^{(F_0, M_F)}(J, t = 0) = C_{F_1}^{(F_0, M_F)} C_{F_2}^{(F_0, M_F)*}, \quad (5)$$

where F_2 stands for total angular momentum also in the electronically excited state.

The time-dependent angular distribution pertinent to the molecular axis is derived as the matrix element of $\hat{\rho}^{(F_0, M_F)}$ with the eigenvectors of the angular coordinate θ (the angle between the space-fixed Z axis and the molecular axis). Since the orientation of the electronic and nuclear spins has not been specified during the observation, the distribution is represented as an average over the spin wave functions as

$$\begin{aligned} P^{(F_0, M_F)}(\theta, t) &= \sum_{M_S, M_I} \langle S M_S | \langle I M_I | \langle \theta | \hat{\rho}^{(F_0, M_F)}(J, t) | \theta \rangle | I M_I \rangle | S M_S \rangle \\ &= \sum_{F_1, F_2} \rho_{F_1, F_2}^{(F_0, M_F)}(J, t) f_{F_1, F_2, M_F}(\theta), \quad (6) \end{aligned}$$

with

$$\begin{aligned} f_{F_1, F_2, M_F}(\theta) &\equiv \sum_{M_S, M_I} \langle I M_I | \langle S M_S | \langle \theta | N \Lambda S J I F_1 M_F \rangle \\ &\quad \times \langle N \Lambda S J I F_2 M_F | \theta \rangle | S M_S \rangle | I M_I \rangle, \quad (7) \end{aligned}$$

which represents a time-independent basis function for the angular distribution. It is further recast with the case (b) basis [see Appendix A, Eqs. (A1)–(A4)] into the following form:

$$\begin{aligned} f_{F_1, F_2, M_F}(\theta) &= \sum_{M_J, M_I} \langle J M_J, I M_I | F_1 M_F \rangle \langle J M_J, I M_I | F_2 M_F \rangle \\ &\quad \times \sum_{M_N, M_S} \langle N M_N, S M_S | J M_J \rangle^2 \frac{2N + 1}{4\pi} [d_{M_N \Lambda}^N(\theta)]^2, \quad (8) \end{aligned}$$

where $\langle \dots, \dots | \dots \rangle$ is the Clebsch-Gordan coefficient and $d_{M_N \Lambda}^N(\theta)$ is the Wigner's d matrix [2]. The angular distribution is expressed as the sum of the time-independent and

dependent terms as

$$P^{(F_0, M_F)}(\theta, t) = \sum_{F_1} \rho_{F_1, F_1}^{(F_0, M_F)}(J, t=0) f_{F_1, F_1, M_F}(\theta) + \sum_{F_1 > F_2} \rho_{F_1, F_2}^{(F_0, M_F)}(J, t=0) f_{F_1, F_2, M_F}(\theta) \times \cos[(\omega_{F_1} - \omega_{F_2})t]. \quad (9)$$

The latter terms, called the quantum beating, are caused by the interferences between eigenstates with different energies.

In the present experimental condition, the initial state is a mixed state with different $|F_0, M_F\rangle$'s. The density matrix of the total system is a weighted sum of those for a single wave packet, as

$$\hat{\rho} = \sum_{F_0, M_F} W_{F_0} \hat{\rho}^{(F_0, M_F)}, \quad (10)$$

where W_{F_0} is the relative distribution for the initial states with $F_0 = 1/2$ and $3/2$. We note that once the density matrix $\hat{\rho}$ is specified, all the physical quantities of the molecular system can be derived from it. In particular, the corresponding angular distribution is given as

$$P(\theta, t) = \sum_{F_0, M_F} W_{F_0} P^{(F_0, M_F)}(\theta, t) = \sum_{F_1, F_2, M_F} \rho_{F_1, M_F, F_2, M_F}(J, t) f_{F_1, F_2, M_F}(\theta), \quad (11)$$

with

$$\rho_{F_1, M_F, F_2, M_F}(J, t) = \sum_{F_0} W_{F_0} \rho_{F_1, F_2}^{(F_0, M_F)}(J, t). \quad (12)$$

Its time dependence is quite similar to Eq. (4) as

$$\rho_{F_1, M_F, F_2, M_F}(J, t) = \rho_{F_1, M_F, F_2, M_F}(J, t=0) e^{-i(\omega_{F_1} - \omega_{F_2})t}. \quad (13)$$

In the present case, all the weights for the six initial states are essentially identical due to the small hfs (with only $\sim 1\%$ difference at even ~ 2 K): $W_{F_0} = 1/6$.

B. Spherical-tensor representation

The hyperfine depolarization is explained as the change of the spatial orientation of the angular momentum \mathbf{J} by the coupling with the nuclear spin \mathbf{I} . To compare our model with the previous formulation [2,3], we introduce the density

matrix of the subsystem $|J, M_J\rangle$. First, we convert the total density matrix from the coupled representation $\rho_{F_1, M_F, F_2, M_F}$ to the uncoupled representation $\rho_{M_{J_1}, M_{I_1}, M_{J_2}, M_{I_2}}$:

$$\begin{aligned} \rho_{M_{J_1}, M_{I_1}, M_{J_2}, M_{I_2}}(J, t) &\equiv \langle JM_{J_1} IM_{I_1} | \hat{\rho} | JM_{J_2} IM_{I_2} \rangle \\ &= \sum_{F_1, F_2, M_F} \langle JM_{J_1}, IM_{I_1} | F_1 M_F \rangle \\ &\quad \times \langle JM_{J_2}, IM_{I_2} | F_2 M_F \rangle \\ &\quad \times \rho_{F_1, M_F, F_2, M_F}(J, t). \end{aligned} \quad (14)$$

To obtain the density matrix in the subspace spanned by the $|J, M_J\rangle$, $\rho_{M_{J_1}, M_{I_1}, M_{J_2}, M_{I_2}}$ is summed up for the subsystem $|I, M_I\rangle$:

$$\rho_{M_{J_1}, M_{J_2}}(J, t) = \sum_{M_I} \rho_{M_{J_1}, M_I, M_{J_2}, M_I}(J, t). \quad (15)$$

Equations (14) and (15) lead to the relation $M_{J_1} + M_I = M_{J_2} + M_I = M_F$, and thus the off-diagonal matrix elements vanish. Similarly, the density matrix in the $|I, M_I\rangle$ subspace is also diagonal. Since the nuclear spin is isotropically distributed at $t = 0$, the matrix elements are given as

$$\rho_{M_{I_1}, M_{I_2}}(J, t=0) = (2I + 1)^{-1} \delta_{M_{I_1}, M_{I_2}}. \quad (16)$$

We next introduce the relationship between the wave packet and the spherical-tensor operator. The q component of the operator of rank k (often called a state multipole moment) is derived from the density matrix elements as [3,62]

$$\begin{aligned} \rho_q^{(k)}(J, t) &= \sqrt{2k+1} \sum_{M_{J_1}, M_{J_2}} (-1)^{J-M_{J_1}} \begin{pmatrix} J & k & J \\ -M_{J_1} & q & M_{J_2} \end{pmatrix} \\ &\quad \times \rho_{M_{J_1}, M_{J_2}}(J, t). \end{aligned} \quad (17)$$

Its inverse transformation is

$$\begin{aligned} \rho_{M_{J_1}, M_{J_2}}(J, t) &= \sum_{k, q} (-1)^{J-M_{J_1}} \sqrt{2k+1} \begin{pmatrix} J & k & J \\ -M_{J_1} & q & M_{J_2} \end{pmatrix} \\ &\quad \times \rho_q^{(k)}(J, t). \end{aligned} \quad (18)$$

Since linear polarization is adopted for excitation in the present case, $q = 0$ and the diagonal elements are only involved in Eqs. (17) and (18). Then Eqs. (14), (15), and (17) provide the transformation from the coupled representation to the spherical tensor:

$$\begin{aligned} \rho_0^{(k)}(J, t) &= \sqrt{2k+1} \sum_{F_0, F_1, F_2, M_F} (-1)^{J+I-M_F} \sqrt{(2F_1+1)(2F_2+1)} W_{F_0} \rho_{F_1, F_2}^{(F_0, M_F)}(J, t) \sum_{M_I} (-1)^{F_1+F_2+I+k+M_F-M_J} \\ &\quad \times \begin{pmatrix} F_2 & I & J \\ -M_F & M_I & M_J \end{pmatrix} \begin{pmatrix} J & k & J \\ M_J & 0 & -M_J \end{pmatrix} \begin{pmatrix} I & J & F_1 \\ M_I & M_J & -M_F \end{pmatrix} \\ &= \sqrt{2k+1} \sum_{F_1, F_2, M_F} (-1)^{J+I-M_F} \sqrt{(2F_1+1)(2F_2+1)} \begin{Bmatrix} F_2 & I & J \\ J & k & F_1 \end{Bmatrix} \begin{pmatrix} k & F_2 & F_1 \\ 0 & -M_F & M_F \end{pmatrix} \rho_{F_1, M_F, F_2, M_F}(J, t). \end{aligned} \quad (19)$$

The inverse transformation at $t = 0$ is provided by using Eqs. (16) and (18) as

$$\begin{aligned} \rho_{F_1, M_F, F_2, M_F}(J, t = 0) &= \sum_{M_{J_1}, M_{J_2}, M_I} \langle JM_{J_1}, IM_I | F_1 M_F \rangle \langle JM_{J_2}, IM_I | F_2 M_F \rangle \rho_{M_{J_1}, M_I, M_{J_2}, M_I}(J, t = 0) \\ &= \sum_{M_{J_1}, M_{J_2}, M_I} \langle JM_{J_1}, IM_I | F_1 M_F \rangle \langle JM_{J_2}, IM_I | F_2 M_F \rangle \rho_{M_{J_1}, M_{J_2}}(J, t = 0) \rho_{M_I, M_I}(J, t = 0) \\ &= \frac{\sqrt{(2F_1 + 1)(2F_2 + 1)}}{2I + 1} \sum_k (-1)^{J+I-M_F} \sqrt{2k+1} \begin{Bmatrix} F_2 & I & J \\ J & k & F_1 \end{Bmatrix} \begin{pmatrix} k & F_2 & F_1 \\ 0 & -M_F & M_F \end{pmatrix} \rho_0^{(k)}(J, t = 0). \end{aligned} \quad (20)$$

Next, we substitute Eq. (13) into Eq. (19) and then replace $\rho_{F_1, M_F, F_2, M_F}(J, t = 0)$ with $\rho_0^{(k)}(J, t = 0)$ by using Eq. (20), to finally have the closure expression for the time propagation of the state multipole moments:

$$\rho_0^{(k)}(J, t) = G^{(k)}(t) \rho_0^{(k)}(J, t = 0) \quad (21)$$

with

$$G^{(k)}(t) \equiv \sum_{F_1, F_2} \frac{(2F_1 + 1)(2F_2 + 1)}{2I + 1} \begin{Bmatrix} F_2 & I & J \\ J & k & F_1 \end{Bmatrix}^2 e^{-i(\omega_{F_1} - \omega_{F_2})t} \quad (22)$$

being just the depolarization coefficient [2,3]. Thus, the present density matrix consideration has confirmed that the spherical-tensor formalism by Orr-Ewing and Zare [2,3] is valid for describing the hyperfine depolarization for hfs eigenstates coherently excited by a linearly polarized light.

By substituting Eq. (20) into Eq. (11), the time-dependent angular distribution is expanded with the state multipole moments as

$$\begin{aligned} P(\theta, t) &= \sum_k \rho_0^{(k)}(J, t) f_0^{(k)}(\theta) \\ &= \sum_k \rho_0^{(k)}(J, t = 0) G^{(k)}(t) f_0^{(k)}(\theta) \end{aligned} \quad (23)$$

with

$$\begin{aligned} f_0^{(k)}(\theta) &\equiv \sum_{M_J} (-1)^{J-M_J} \langle JM_J, J - M_J | k 0 \rangle \\ &\times \sum_{M_N, M_S} \langle NM_N, SM_S | JM_J \rangle^2 \frac{2N + 1}{4\pi} [d_{M_N \Lambda}^N(\theta)]^2. \end{aligned} \quad (24)$$

The basis function for the angular distribution, now expanded in state multipoles, is further recast after some angular momentum algebra, as shown in Appendix C, into a very concise form as

$$\begin{aligned} f_0^{(k)}(\theta) &= (-1)^{J+S} \frac{(2N + 1)(2J + 1)\sqrt{2k + 1}}{4\pi} \\ &\times \begin{Bmatrix} N & S & J \\ J & k & N \end{Bmatrix} \begin{pmatrix} k & N & N \\ 0 & -\Lambda & \Lambda \end{pmatrix} P_k(\cos \theta), \end{aligned} \quad (25)$$

which is simply proportional to the Legendre polynomial of rank k , $P_k(\cos \theta)$. The expression given in Eq. (23) along with Eq. (25) can be directly compared to the observed time-dependent angular distribution.

III. EXPERIMENT

Details of the experimental setup have been described in the previous report [59]. Briefly, a gaseous mixture of $\sim 0.7\%$ NO diluted in helium was expanded into a vacuum chamber from an Even-Lavie pulsed valve (repetition rate at 250 Hz; back pressure: 2 MPa). The molecular beam of the adiabatically cooled sample (with rotational temperature of ~ 2 K), with its propagation direction set here along the Z axis, was crossed at right angles with the pump and probe laser pulses, which counterpropagated to each other (along the Y axis). The ns ultraviolet pump pulse was delivered as second harmonics (226 nm, ~ 20 nJ, pulse width < 10 ns, linewidth ~ 1 GHz, repetition rate at 250 Hz) of the output of a dye laser (Sirah, Allegro, with coumarin 450 dye). The near-infrared intense probe pulse was provided as an output of a Ti^+ sapphire multipass amplifier (Quantronix, Odin II HE, ~ 800 nm, pulse width ~ 80 fs, repetition rate at 1 kHz). The pump pulse was linearly polarized through a half-wave plate and a Glan laser

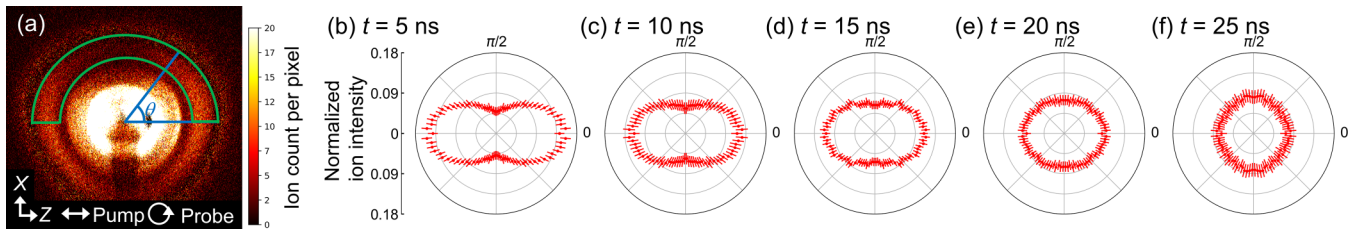


FIG. 2. Distributions of N^+ fragments from the excited NO molecules: (a) The spatial distribution after correction to the circular shape of the subtracted image. The annotated half circle marks the inner-shell region analyzed in this work. (b–f) Time-dependent angular distributions derived from the observed images for each pump-probe delay. Data per 4° are plotted as red dots with three times standard deviation indicated as red bars.

TABLE I. Retrieved state-multipole moments $\rho_0^{(k)}(J, t)$. Numbers in parentheses are the 3σ standard deviation of the fit, in units of the last quoted digit.

t (ns)	$k = 0$	$k = 2$
5	0.503 (10)	-0.410 (8)
10	0.501 (13)	-0.250 (11)
15	0.500 (9)	-0.187 (8)
20	0.500 (11)	-0.066 (10)
25	0.500 (15)	0.019 (13)

prism and was focused onto the molecular beam by a lens ($f = 250$ mm). Its polarization direction was set along the Z axis, perpendicular to the time-of-flight (TOF) direction (along the X axis). The probe pulse was circularly polarized by passing through a series of a half-wave plate, a pair of reflection-type prism polarizers, and a quarter-wave plate, and finally focused onto the molecular beam by another lens ($f = 150$ mm). The timings of the pump and probe pulses and the valve opening were controlled by a digital delay generator. Spatial distributions of ions generated by the irradiation of light pulses were recorded as tomographic images (in the ZX plane) by space-slice ion imaging [39,46,47].

The spatial overlap between the pump and probe pulses had to be optimized for each record of images with different pump-probe delays, since molecules excited by the pump pulses were moved by ~ 10 μm during a few tens of ns due to the molecular-beam translation. The best overlap of the two pulses was achieved by finding the substantial enhancement of NO^+ generation, while the intensities of both pulses were set so low that negligible NO^+ ions were generated by pump or probe pulse only. Then, the pump-pulse intensity was raised to increase the numbers of excited molecules within the range of a very low level of two-photon ionization signals by the pump pulse alone. The probe intensity was adjusted to give high contrast of the N^+ signals enhanced by the pump against those with the probe pulse alone. The optimized pulse

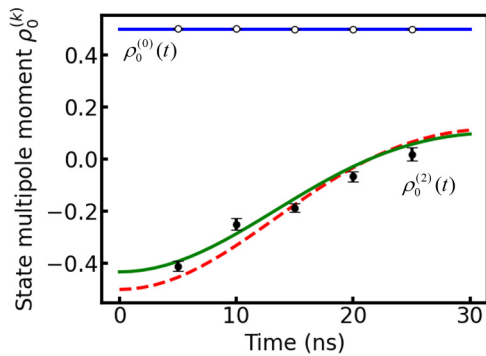


FIG. 3. The state-multipole moments plotted against the delay time. Experimentally determined $\rho_0^{(0)}(J, t)$ and $\rho_0^{(2)}(J, t)$ at each delay time are indicated as open circles and dots, respectively, with black bars as three times standard deviation of the fit. Blue and green lines are results of the global fit to the determined $\rho_0^{(0)}(J, t)$ and $\rho_0^{(2)}(J, t)$, respectively. Theoretical predictions for $\rho_0^{(k)}(J, t)$ are given as a red broken line.

TABLE II. State-multipole moments $\rho_0^{(k)}(J, t = 0)$.

	Obs. ^a	Theory
$k = 0$	0.501 (2)	0.5
$k = 2$	-0.44 (9)	-0.5

^aStatistical uncertainties (3σ) are represented in parentheses in units of the last quoted digit.

energy was ~ 200 μJ , which was fixed for a series of image recordings.

The image recorded with the pump and probe pulses contained ion signals from the ground-state molecules as well as from the excited molecules. The latter signals were much larger than the former, although the relative population in the excited state was estimated to be only $\sim 10\%$ [59]. After subtracting the background signals recorded with the probe pulse only, we analyzed the spatial distribution of N^+ fragments from the excited NO molecules. The signals were distributed in an elliptical shape because the ion cloud was kept constant along the acceleration direction (along the X axis) while it expanded along the perpendicular direction (along the Z axis). The ion image was least-squares fitted to determine the elliptical parameters (i.e., the center position and the ellipticity) and its Z/X aspect ratio was corrected to give a circular shape that represents the angular distribution. The resultant image of fragment ions can be regarded as a 2D section of the three-dimensional (3D) probability distribution pertinent to the molecular axis in the laboratory frame. This is mainly owing to the isotropic ionization efficiency within the plane of detection by using the circularly polarized probe-laser field; in addition the axial recoil approximation was valid and the effect of the dynamical alignment induced by the probe pulse was marginal in the present experimental condition [46,47,59].

The angular distribution for the ground-state molecules should be isotropic due to their random orientation as an initial distribution. Still, the images of the observed background signals showed some fluctuation, most probably due to the spatial variation in the detecting efficiency of the PSD. This

TABLE III. Density matrix elements, $\rho_{F_1, M_{F_1}, F_2, M_{F_2}}(J, t = 0)$, for the coupled-presentation basis. Plus-minus and minus-plus values of the elements correspond to the plus-minus values of M_F .

(F_1, F_2, M_F)	Obs. ^a	Theory	Obs.–theory
(1/2, 1/2, $\pm 1/2$)	0.0835 (2)	0.0833	0.000
(1/2, 3/2, $\pm 1/2$)	∓ 0.066 (14)	∓ 0.0745	± 0.008
(1/2, 5/2, $\pm 1/2$)	-0.033 (7)	-0.0373	0.004
(3/2, 3/2, $\pm 1/2$)	0.098 (3)	0.1000	-0.002
(3/2, 5/2, $\pm 1/2$)	∓ 0.030 (6)	∓ 0.0333	± 0.003
(5/2, 5/2, $\pm 1/2$)	0.143 (12)	0.1500	-0.007
(3/2, 3/2, $\pm 3/2$)	0.069 (3)	0.0667	0.002
(3/2, 5/2, $\pm 3/2$)	∓ 0.073 (15)	∓ 0.0816	± 0.008
(5/2, 5/2, $\pm 3/2$)	0.098 (3)	0.1000	-0.002
Norm	0.982 (43)	1.0000	-0.018

^aStatistical uncertainties (3σ) are represented in parentheses in units of the last quoted digit.

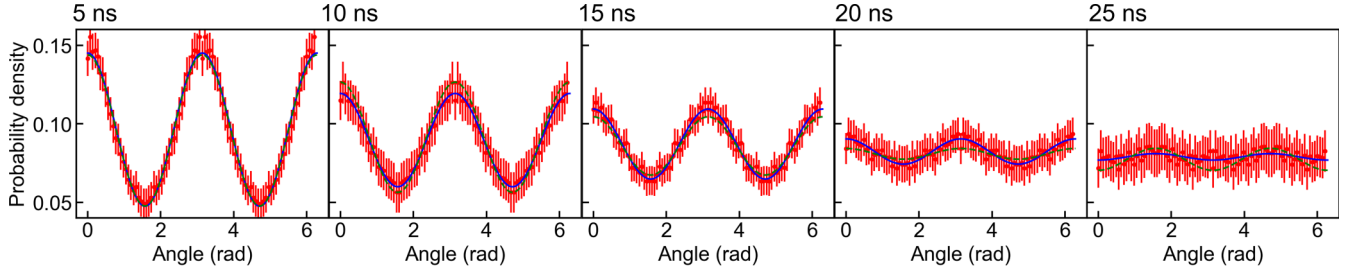


FIG. 4. The angular distributions at each delay time: The experimental values are indicated as red dots with 3σ statistical errors (red bars), calculated with the determined $\rho_0^{(0)}(J, t)$ and $\rho_0^{(2)}(J, t)$ at each delay time as blue lines, calculated for the global fit as green broken lines, and the theoretical prediction as black dashed-dotted lines.

positional detection variation was corrected by normalization of the excited-state signals with the background signals and right-left symmetrization. Parts of the images of the N^+ signals were overlapped with other ions, e.g., NO^{2+} and O^+ , in the region for larger TOFs (or smaller X positions). Thus, the upper (or larger X) half of the circular signals was only used to obtain the angular distribution to avoid the interferences. Given that the 3D angular distribution should be axially symmetric around the polarization direction, the images of each delay were normalized by the integration around the symmetry axis.

IV. RESULTS AND DISCUSSION

Figure 2(a) shows a typical ion image of N^+ fragments from excited NO molecules. There appear three different velocity components: the central part as well as two annular regions. In the present study, the angular distributions were derived from the signals in the inner-ring region, as shown in the green half circle region in Fig. 2(a), since the signal counts are much larger and more enhanced by the pump pulse than those in the outer-ring region. The angular distributions $P(\theta, t)$ at each pump-probe delay are shown as red dots in the polar plots [Figs. 2(b)–2(f)], with the experimental statistical error of three times standard deviation (3σ , with σ being evaluated from the square root of the ion counts) indicated as red bars. Small standard deviation and high angular resolution express the benefit of high data throughput realized by using our ion-imaging apparatus [46,47].

As shown in the sequence with the delay time from 0 to 25 ns [Figs. 2(b)–2(f)], the angular distribution pertinent to the molecular-axis direction, initially concentrated along the pump polarization (horizontal) direction, gradually grows isotropic. This time evolution of $P(\theta, t)$ is represented as a linear combination of products of the angular- and time-dependent terms $f_0^{(k)}(\theta)$ and $\rho_q^{(k)}(J, t)$, respectively, as given in Eq. (23). The latter term, called the state-multipole moment, is further recast as a product of the initial value $\rho_0^{(k)}(J, t=0)$ and the time-dependent depolarization coefficient $G^{(k)}(t)$, as given in Eq. (21). For the excitation to $J = 3/2$, the rank k of the state multipole should be ≤ 3 , to satisfy the triangle condition in Eq. (17). In addition, terms with odd k do not contribute due to the vanishing $3-j$ symbol in Eq. (25) with $\Lambda = 0$. Thus, terms with $k = 0$ and 2 are only considered for the time-dependent angular distribution observed in the present

study. For $k = 0$, the triangle rule for the $6-j$ symbol in Eq. (22) allows only $F_1 = F_2$; then $G^{(0)}$ becomes stationary. For $k = 2$, $|F_1 - F_2| \leq 2$, and $G^{(2)}$ shows time evolution. The angular basis functions in Eq. (25) are given as $f_0^{(0)}(\theta) = 1/(2\pi)$ and $f_0^{(2)}(\theta) = -P_2(\cos\theta)/(2\pi)$ in the present case; i.e., $N = 2$, $S = 1/2$, $J = 3/2$, and $\Lambda = 0$. Then, the angular distribution $P(\theta, t)$ points to the horizontal or vertical direction when $\rho_0^{(2)}(J, t)$ is negative or positive, respectively. It is noted that the angular momentum vector \mathbf{J} is approximately perpendicular to the molecular axis and it exhibits alignment or antialignment against the laser polarization direction for positive or negative values of $\rho_0^{(2)}(J, t)$.

The angular distribution is subjected to least-squares regression to Eq. (23) with $\rho_0^{(0)}(J, t)$ and $\rho_0^{(2)}(J, t)$ taken as variables at each delay time t . The results are listed in Table I and also plotted in Fig. 3. Reproduction of the angular distribution is satisfactorily good as shown in Fig. 4, where the experimentally obtained $P(\theta, t)$ is compared with that calculated from the determined state multipoles. As expected, $\rho_0^{(0)}(J, t)$ remains constant (~ 0.5), while $\rho_0^{(2)}(J, t)$ gradually changes from ca -0.4 to 0 as the delay becomes larger. Then, the state-multipole moments thus determined at each delay time are subjected to the global fit by adopting Eq. (21) to evaluate the initial values of $\rho_0^{(k)}(J, t=0)$ for $k = 0$ and 2. Here $G^{(k)}(t)$ is calculated with the hfs frequencies reported previously [51]. The determined state-multipole moments at $t = 0$ are listed in Table II. The stationary $k = 0$ component is determined with small statistical uncertainty (3σ is less than 0.1%). The $k = 2$ component shows a larger uncertainty (3σ reaches almost 20%), but the deviations at each delay time from the fitting curve are within acceptable ranges, as shown in Fig. 3.

Once the state-multipole moments at $t = 0$ have been determined, all the density matrix elements with the coupled-presentation basis, $\rho_{F_1, M_F, F_2, M_F}(J, t=0)$, are experimentally retrieved by using Eq. (20). Their statistical uncertainties are also evaluated from 3σ of the state-multipole moments. The results are listed in Table III. The norm of the density matrix is only 0.2% smaller than unity. This fact validates the present analysis.

When the electronic excitation is well within the weak field limit, the wave-packet expansion coefficients for the (F_0, M_F) initial state, $C_{F_1}^{(F_0, M_F)}$, are proportional to the transition probabilities as mentioned before. Then, they are theoretically predicted by using Eq. (2). The density matrix elements at

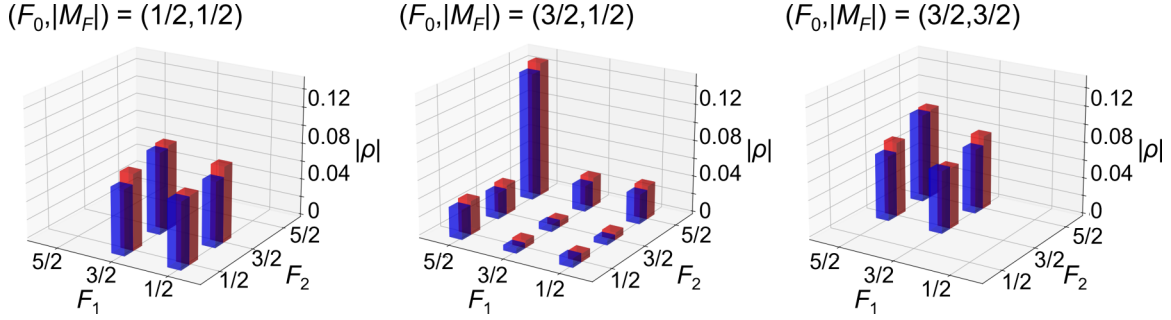


FIG. 5. The 3D bar charts of the density matrix elements $\rho_{F_1, F_2}^{(F_0, M_F)}(J, t = 0)$, retrieved from observation (blue), and calculated for completely coherent wave packets (red).

$t = 0$ are also calculated from the theoretical coefficients, by adopting Eqs. (5) and (12). The results are also listed in Table III.

By using the calculated density matrix elements, the state-multipole moments are predicted by Eq. (19), as listed in Table II. In the comparison with the experimental values, the stationary term with $k = 0$ shows quite a good matchup. In contrast, the time-dependent $k = 2$ term exhibits small but notable deviation. The experimental value is smaller than the predicted one by almost 15%. We note that the prediction relies on fully coherent excitation to create the wave packets. Since the excitation source in the present experiments is a pulsed dye laser, which operates at multi-longitudinal-mode oscillation, the coherence in the resultant wave packets may be degraded to some extent, to give smaller amplitude in the $k = 2$ term. In fact, the density matrix for $M_F = \pm 3/2$ exclusively comes from the $F_0 = 3/2$ initial state, and the following equation should be held for completely coherent excitation:

$$\frac{|\rho_{3/2, \pm 3/2, 5/2, \pm 3/2}|}{\sqrt{\rho_{3/2, \pm 3/2, 3/2, \pm 3/2} \rho_{5/2, \pm 3/2, 5/2, \pm 3/2}}} = 1, \quad (26)$$

but the experimental ratio is $\sim 0.88(3)$, indicating the incoherent nature of the systems.

The density matrix elements, $\rho_{F_1, M_F, F_2, M_F}(J, t = 0)$, are the sums of the components, $\rho_{F_1, F_2}^{(F_0, M_F)}(J, t = 0)$, for the initial states, as represented in Eq. (12). The values of $\rho_{F_1, F_2}^{(F_0, M_F)}(J, t = 0)$ can be retrieved with several assumptions as follows. First, the weights, W_{F_0} , for each initial state are to be the same. Second, the degree of incoherence in the off-diagonal terms is assumed to be the same, i.e.,

$$\frac{|\rho_{F_1, F_2}^{(F_0, M_F)}|}{\sqrt{\rho_{F_1, F_1}^{(F_0, M_F)} \rho_{F_2, F_2}^{(F_0, M_F)}}} = x \quad (27)$$

to be held for any F_0, F_1, F_2 , and M_F , with a single value of x , which is an empirical parameter to describe the extent of incoherence. Here the sign of the off-diagonal matrix elements is set to be consistent to Eq. (2); (i.e.), the sign is positive or negative when $F_0 + F_1 - M_F - S$ is even or odd.

The retrieved density matrix elements, $\rho_{F_1, F_2}^{(F_0, M_F)}(J, t = 0)$, are represented as 3D bar charts in Fig. 5, along with the theoretically predicted values for the completely coherent situation. The results are also tabulated in Table IV in Appendix D. The value of x is found to be 0.89. It is noted that all the diagonal and off-diagonal terms for the initial $(F_0, M_F) =$

$(1/2, \pm 1/2)$ and $(3/2, \pm 3/2)$ states are comparable, while the diagonal $(F_1, F_2) = (5/2, 5/2)$ terms dominate over other terms for $(F_0, M_F) = (3/2, \pm 1/2)$. That means the former two are close to maximally coherent states, while the latter is not.

Since the density matrix has been experimentally derived, any physical quantity of the system can be evaluated. First, we reconstruct the time evolution of the molecular-axis angular distributions of subsystems for the initial $(F_0, M_F) = (1/2, \pm 1/2), (3/2, \pm 1/2), (3/2, \pm 3/2)$ states [Figs. 6(a)–6(c)] as well as that for the total system [Fig. 6(d)]. All the distributions of the subsystems exhibit the same shape at $t = 0$, and they evolve differently from each other. As shown in Figs. 6(a) and 6(c), the distributions from $(1/2, \pm 1/2)$ and $(3/2, \pm 3/2)$ clearly show an antialignment maximum at around 40 and 30 ns, respectively, while that from $(3/2, \pm 1/2)$ stays aligned up to 50 ns [Fig. 6(b)]. The large time dependence in the former two systems is due to their maximally coherent nature while the weak modulation in the latter system is a consequence from the predominance of a single diagonal term, as just mentioned. Because of the different behaviors of each subsystem, evolution of the total distribution is slow and moderate.

TABLE IV. Density matrix elements, $\rho_{F_1, F_2}^{(F_0, M_F)}(J, t = 0)$. Plus-minus and minus-plus values of the elements correspond to the plus-minus values of M_F .

(F_0, M_F)	(F_1, F_2)	Obs. ^a	Theory	Obs.–theory
$(1/2, \pm 1/2)$	$(1/2, 1/2)$	0.0737 (2)	0.074	0.000
	$(1/2, 3/2)$	∓ 0.072 (13)	∓ 0.083	± 0.011
	$(3/2, 3/2)$	0.090 (3)	0.093	–0.003
	Norm	0.328 (6)	0.333	–0.005
$(3/2, \pm 1/2)$	$(1/2, 1/2)$	0.00979 (3)	0.009	0.001
	$(1/2, 3/2)$	± 0.006 (1)	± 0.008	∓ 0.002
	$(1/2, 5/2)$	–0.033 (7)	–0.037	0.004
	$(3/2, 3/2)$	0.0098 (3)	0.007	0.003
	$(3/2, 5/2)$	∓ 0.030 (6)	∓ 0.033	± 0.003
	$(5/2, 5/2)$	0.143 (13)	0.150	–0.007
	Norm	0.321 (26)	0.333	–0.012
$(3/2, \pm 3/2)$	$(3/2, 3/2)$	0.069 (3)	0.067	0.002
	$(3/2, 5/2)$	∓ 0.073 (15)	∓ 0.082	± 0.009
	$(5/2, 5/2)$	0.098 (3)	0.100	–0.002
	Norm	0.334 (12)	0.333	0.001

^aStatistical uncertainties are represented in parentheses in units of the last quoted digit.

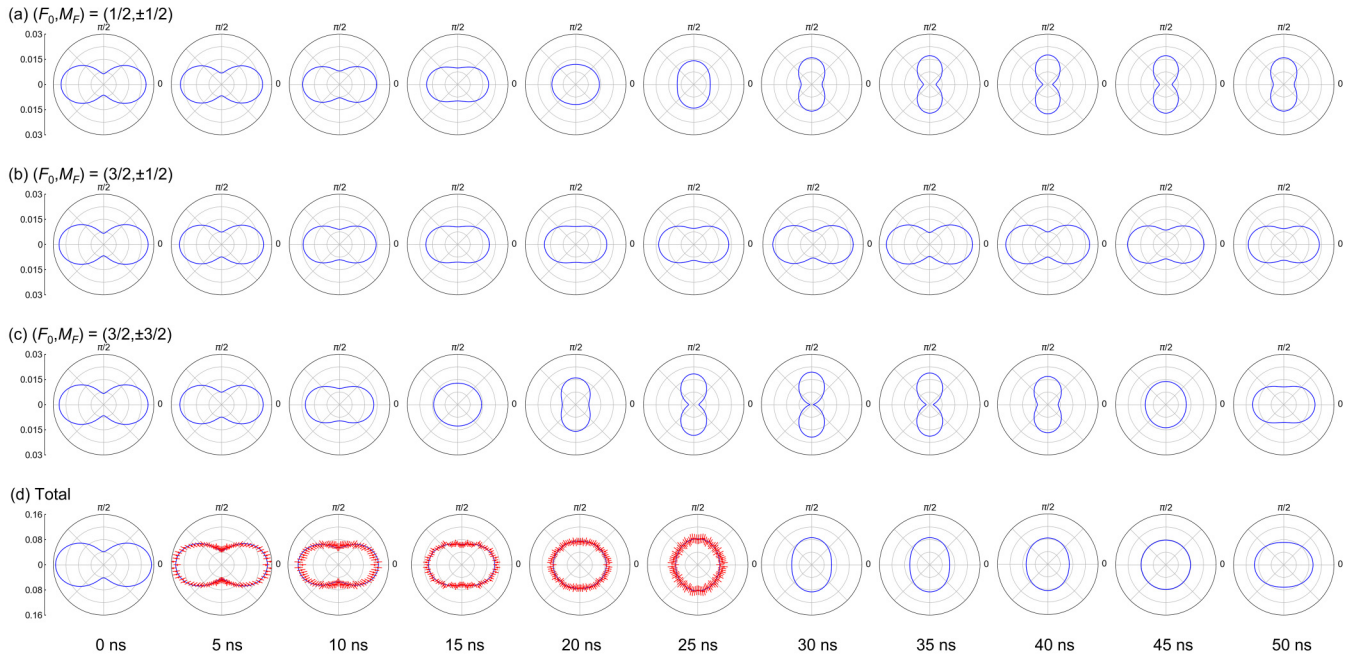


FIG. 6. Reconstructed molecular-axis angular distributions. (a–c) for the initial states $(F_0, M_F) = (1/2, \pm 1/2)$, $(3/2, \pm 1/2)$, and $(3/2, \pm 3/2)$, respectively. (d) Total reconstructed distribution (blue lines) with observed data (red dots with error bars).

Next, we discuss longer-time dynamics. Here the time-dependent alignment parameter, $\langle \cos^2\theta \rangle(t)$, is evaluated up to $1 \mu\text{s}$, as shown in Fig. 7. The parameter exhibits almost full revival at $t = 800 \text{ ns}$. The value at this timing (and also $t = 0$) is the largest, 0.451. The revival time is ascribed as nearly integral multiples (10, 13, and 23, respectively) of the three beating periods (80.0, 61.5, and 34.8 ns) between hfs components [51]. The alignment parameter is symmetric with respect to the half revival (400 ns), and at several timings until then, it becomes maxima at $t = 68, 131, 177, 244, 312,$ and 378 ns , with its values of 0.429, 0.379, 0.413, 0.449, 0.431, and 0.396, respectively. The minima appear at $t = 33, 94, 153, 213, 278, 341,$ and 400 ns , with the values of 0.306, 0.337, 0.345, 0.314, 0.301, 0.326, and 0.348, respectively. Some of the timings are also nearly integral multiples of the three hfs beating periods. For instance, 244 and 312 ns correspond to (3, 4, 7) and (4, 5, 9), respectively. Aligned or antialigned molecular ensembles

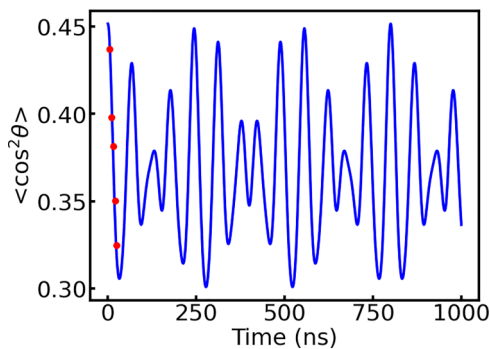


FIG. 7. Time evolution of the alignment parameter, $\langle \cos^2\theta \rangle$, from the experiments (red circles), and calculated by the reconstructed density matrix (blue line).

appearing a few hundred ns after their creation will be utilized in several dynamical studies, e.g., on photodissociation, but the time window for its utility is restricted by the deactivation of NO ($A^2\Sigma^+$, $v = 0$), the fluorescence lifetime of which is $\sim 200 \text{ ns}$ [63–65].

V. CONCLUSION

We report here detailed tracking of time-dependent molecular-axis distribution of nitric oxide (NO) molecules after the excitation into a single rotational level ($A^2\Sigma^+$, $v = 0$, $N = 2$, $J = 3/2$). The angular distribution has been recorded by a space-sliced ion-imaging apparatus coupled with a circularly polarized intense laser pulse as a probe [60]. This experimental setup affords us nonmathematical tomographic imaging with high collecting availability of signal ions. As the pump-probe timing is delayed, the molecular-axis distribution evolves from alignment to antialignment. This is a clear manifestation of rotational angular momentum depolarization by the hyperfine interaction with the ^{14}N nuclear spin. The time-dependent state multipole moment is retrieved experimentally and the density matrix on a coupled basis is reconstructed. The present results enable us to discuss the incoherence of the created molecular system. By utilizing the retrieved density matrix, any physical quantity can be evaluated. We have demonstrated it here by breaking down the time-dependent total angular distribution into those for each initial state and by estimating long-time alignment and antialignment dynamics to show the characteristic revival structure.

ACKNOWLEDGMENTS

This work was financially supported by JSPS KAKENHI (Grants No. JP18H03897, No. JP21K18938, No.

JP21H05434, No. JP22H00312, and No. JP22K18327), the Core-to-Core program (Grant No. JPJSCCA20210004), and the Yoshinori Ohsumi Fund for Fundamental Research in TokyoTech.

APPENDIX A: BASIS OF NITRIC OXIDE IN $X^2\Pi_{1/2}$ AND $A^2\Sigma^+$

The molecular wave function of NO ($A^2\Sigma^+$) is defined as

$$|A^2\Sigma^+, v, N\Lambda S J I F M_F\rangle \equiv |n\Lambda\rangle|v\rangle|N\Lambda S J I F M_F\rangle, \quad (\text{A1})$$

where $|n\Lambda\rangle$ and $|v\rangle$ are the electronic and vibrational parts of the state vector, respectively, and $|N\Lambda S J I F M_F\rangle$ is the basis of Hund's case ($b_{\beta J}$), which is described as

$$|N\Lambda S J I F M_F\rangle = \sum_{M_J, M_I} \langle J M_J, I M_I | F M_F \rangle |N\Lambda S J M_J\rangle |I M_I\rangle, \quad (\text{A2})$$

with $|I M_I\rangle$ being the nuclear spin part, and $|N\Lambda S J M_J\rangle$ is the basis of Hund's case (b). It is further recast as

$$|N\Lambda S J M_J\rangle = \sum_{M_N, M_S} \langle N M_N, S M_S | J M_J \rangle |N\Lambda M_N\rangle |S M_S\rangle, \quad (\text{A3})$$

with $|S M_S\rangle$ being the electronic spin part, and the $|N\Lambda M_N\rangle$ with the Wigner D matrix, as

$$\begin{aligned} |N\Lambda M_N\rangle &= \psi_{N,\Lambda, M_N}(\theta, \phi) = \langle \theta, \phi, \chi = 0 | N\Lambda M_N \rangle \\ &= \left(\frac{2N+1}{4\pi} \right)^{\frac{1}{2}} D_{M_N, \Lambda}^{(N)*}(\phi, \theta, \chi = 0). \end{aligned} \quad (\text{A4})$$

The wave function of NO ($X^2\Pi_{1/2}$) is defined as

$$\begin{aligned} |X^2\Pi_{1/2}, v, S\Sigma, \bar{\Omega} J I F M_F, \varepsilon\rangle \\ \equiv |v\rangle[|n\Lambda, S\Sigma, \bar{\Omega} J I F M_F\rangle \\ + \varepsilon|n-\Lambda, S-\Sigma, -\bar{\Omega} J I F M_F\rangle], \end{aligned} \quad (\text{A5})$$

where $\varepsilon = +1$ or -1 is the label of parity, $\bar{\Omega}$ is the absolute value of Ω , and $|n\Lambda, S\Sigma, \Omega J I F M_F\rangle$ is the basis of Hund's case (a_{β}) which is described as

$$\begin{aligned} |n\Lambda, S\Sigma, \Omega J I F M_F\rangle \\ = \sum_{M_I} \langle J M_J, I M_I | F M_F \rangle |n\Lambda, S\Sigma, J\Omega M_J\rangle |I M_I\rangle, \end{aligned} \quad (\text{A6})$$

with

$$|n\Lambda, S\Sigma, J\Omega M_J\rangle = |n\Lambda\rangle|S\Sigma\rangle|J\Omega M_J\rangle, \quad (\text{A7})$$

where $|S\Sigma\rangle$ and $|J\Omega M_J\rangle$ are the electronic spin part written in the molecular frame and the basis of Hund's case (a), respectively. The rotational part is represented as

$$\begin{aligned} |J\Omega M_J\rangle &= \psi_{J,\Omega, M_J}(\theta, \phi) = \langle \theta, \phi, \chi = 0 | J\Omega M_J \rangle \\ &= \left(\frac{2J+1}{4\pi} \right)^{\frac{1}{2}} D_{M_J, \Omega}^{(J)*}(\phi, \theta, \chi = 0). \end{aligned} \quad (\text{A8})$$

The relationship between case (a) and case (b) is

$$|n\Lambda, S\Sigma, J\Omega M_J\rangle = \sum_{N, \Lambda} \langle N\Lambda, S\Sigma | J\Omega \rangle |N\Lambda S J M_J\rangle. \quad (\text{A9})$$

Using Eq. (A9), we can convert the case (a) basis to the case (b) basis.

APPENDIX B: COEFFICIENT $C_{F_1}^{(F_0, M_F)}$ OF THE EIGENSTATE $|A^2\Sigma^+, N\Lambda S J I F M_F\rangle$

The electric dipole interaction is written as $\hat{H}' = \hat{\mu} \cdot \hat{\mathbf{E}} = \sum_p \mu_{-p}^{(1)} E_p^{(1)} = \sum_{p,q} D_{-pq}^{(1)*} \mu_q^{(1)} E_p^{(1)}$. Here the electric dipole moment μ and the laser electric field \mathbf{E} are represented as spherical-tensor operators of rank 1, $\mu_q^{(1)}$ and $E_p^{(1)}$, respectively, with the suffix p and q ($=0$ or ± 1) specifying the space-fixed (lab) frame and the molecular-fixed frame, and $D_{pq}^{(1)*}$ is the complex conjugate of the Wigner D matrix [2].

The coefficient of the excited eigenstate is proportional to the interaction matrix element, under the first-order perturbation framework, because the F dependencies of the electronic excitation energy can be securely ignored,

$$C_{F_1}^{(F_0, M_F)} = \frac{\langle A^2\Sigma^+, N_1\Lambda_1 S J_1 I F_1 M_F | \hat{H}' | X^2\Pi, S\Sigma, \bar{\Omega} J_0 I F_0 M_F, \varepsilon \rangle}{\hbar \Delta \omega}, \quad (\text{B1})$$

with $\Delta \omega$ being the angular frequency for the $A^2\Sigma^+ - X^2\Pi_{1/2} R_{21}(1/2)$ transition of NO.

Using Eq. (A5), the matrix element is written as

$$\begin{aligned} \langle A^2\Sigma^+, N_1\Lambda_1 S J_1 I F_1 M_F | \hat{H}' | X^2\Pi, S\Sigma, \bar{\Omega} J_0 I F_0 M_F, \varepsilon \rangle \propto \langle n_1\Lambda_1, N_1\Lambda_1 S J_1 I F_1 M_F | \hat{H}' | n_0\Lambda_0, S\Sigma, \bar{\Omega} J_0 I F_0 M_F \rangle \\ + \varepsilon \langle n_1\Lambda_1, N_1\Lambda_1 S J_1 I F_1 M_F | \hat{H}' | n_0-\Lambda_0, S-\Sigma, -\bar{\Omega} J_0 I F_0 M_F \rangle. \end{aligned} \quad (\text{B2})$$

The matrix elements in Eq. (B2) are recast as

$$\langle n_1\Lambda_1, N_1\Lambda_1 S J_1 I F_1 M_F | \hat{H}' | n_0\Lambda_0, S\Sigma, \bar{\Omega} J_0 I F_0 M_F \rangle = \sum_p E_p^{(1)} \sum_q \langle n_1\Lambda_1 | \mu_q^{(1)} | n_0\Lambda_0 \rangle \langle N_1\Lambda_1 S J_1 I F_1 M_F | D_{-pq}^{(1)*} | S\Sigma, \bar{\Omega} J_0 I F_0 M_F \rangle. \quad (\text{B3})$$

We can use the two relationships,

$$\langle n_1\Lambda_1 = 0 | \mu_{\mp 1}^{(1)} | n_0\Lambda_0 = \pm 1 \rangle = \langle n_1\Lambda_1 = 0 | \mu_{\pm 1}^{(1)} | n_0\Lambda_0 = \mp 1 \rangle, \quad (\text{B4})$$

and

$$\langle N_1\Lambda_1 S J_1 I F_1 M_F | D_{-pq}^{(1)*} | S-\Sigma, -\bar{\Omega} J_0 I F_0 M_F \rangle = (-1)^{J_0+S+N_1+1} \langle N_1\Lambda_1 S J_1 I F_1 M_F | D_{-pq}^{(1)*} | S\Sigma, \bar{\Omega} J_0 I F_0 M_F \rangle. \quad (\text{B5})$$

Then, the matrix element in Eq. (B2) is given as

$$\begin{aligned} & \langle A^2 \Sigma^+, N_1 \Lambda_1 S J_1 I F_1 M_F | \hat{H}' | X^2 \Pi, S \Sigma, \bar{\Omega} J_0 I F_0 M_F, \varepsilon \rangle \\ & \propto \{1 - \varepsilon(-1)^{J_0+S+N_1+1}\} \langle n_1 \Lambda_1, N_1 \Lambda_1 S J_1 I F_1 M_F | \hat{H}' | n_0 \Lambda_0, S \Sigma, \bar{\Omega} J_0 I F_0 M_F \rangle. \end{aligned} \quad (\text{B6})$$

The matrix element appearing in Eq. (B6) can be recast as

$$\begin{aligned} & \langle N_1 \Lambda_1 S J_1 I F_1 M_F | D_{-pq}^{(1)*} | S \Sigma, \bar{\Omega} J_0 I F_0 M_F \rangle = (-1)^{F_1-M_F} \begin{pmatrix} F_1 & 1 & F_0 \\ -M_F & -p & M_F \end{pmatrix} \langle N_1 \Lambda_1 S J_1 I F_1 | D_q^{(1)*} | S - \Sigma, -\bar{\Omega} J_0 I F_0 \rangle \\ & = (-1)^{F_0+F_1+J_1+I+1-M_F} \sqrt{(2F_0+1)(2F_1+1)} \begin{Bmatrix} J_1 & F_1 & I \\ F_0 & J_0 & k \end{Bmatrix} \begin{pmatrix} F_1 & 1 & F_0 \\ -M_F & -p & M_F \end{pmatrix} \langle N_1 \Lambda_1 S J_1 | D_q^{(1)*} | S - \Sigma, -\bar{\Omega} J_0 \rangle \\ & = \sum_{N_0} (-1)^{F_0+F_1+J_1+N_0+I-S+1-\bar{\Omega}-M_F} \sqrt{(2F_0+1)(2F_1+1)(2N_0+1)} \\ & \quad \times \begin{Bmatrix} J_1 & F_1 & I \\ F_0 & J_0 & 1 \end{Bmatrix} \begin{pmatrix} F_1 & 1 & F_0 \\ -M_F & -p & M_F \end{pmatrix} \begin{pmatrix} N_0 & S & J_0 \\ \Lambda_0 & -\Sigma & \bar{\Omega} \end{pmatrix} \langle N_1 \Lambda_1 S J_1 | D_q^{(1)*} | N_0 \Lambda_0 S J_0 \rangle \\ & = \sum_{N_0} (-1)^{F_0+F_1+J_0+J_1+N_0+N_1+I+2-\bar{\Omega}-M_F} \sqrt{(2F_0+1)(2F_1+1)(2J_0+1)(2J_1+1)(2N_0+1)} \\ & \quad \times \begin{Bmatrix} J_1 & F_1 & I \\ F_0 & J_0 & 1 \end{Bmatrix} \begin{Bmatrix} N_1 & J_1 & S \\ J_0 & N_0 & 1 \end{Bmatrix} \begin{pmatrix} F_1 & 1 & F_0 \\ -M_F & -p & M_F \end{pmatrix} \begin{pmatrix} N_0 & S & J_0 \\ \Lambda_0 & -\Sigma & \bar{\Omega} \end{pmatrix} \langle N_1 \Lambda_1 | D_q^{(1)*} | N_0 \Lambda_0 \rangle \\ & = \sum_{N_0} (-1)^{F_0+F_1+2J_0+J_1+2N_0+2N_1+I+S+2-\bar{\Omega}-\Lambda_1-M_F} \sqrt{(2F_0+1)(2F_1+1)(2J_0+1)(2J_1+1)(2N_0+1)} \\ & \quad \times \begin{Bmatrix} J_1 & F_1 & I \\ F_0 & J_0 & 1 \end{Bmatrix} \begin{Bmatrix} N_1 & J_1 & S \\ J_0 & N_0 & 1 \end{Bmatrix} \begin{pmatrix} F_1 & 1 & F_0 \\ -M_F & -p & M_F \end{pmatrix} \begin{pmatrix} N_0 & S & J_0 \\ -\Lambda_0 & \Sigma & -\bar{\Omega} \end{pmatrix} \begin{pmatrix} N_1 & 1 & N_0 \\ -\Lambda_1 & q & \Lambda_0 \end{pmatrix} \langle N_1 | D_q^{(1)*} | N_0 \rangle \\ & = (-1)^{F_0+F_1+J_0+2J_1+I-2\Lambda_1-M_F} \sqrt{(2F_0+1)(2F_1+1)(2J_0+1)(2J_1+1)(2N_1+1)} \begin{Bmatrix} J_1 & F_1 & I \\ F_0 & J_0 & 1 \end{Bmatrix} \begin{pmatrix} F_1 & 1 & F_0 \\ -M_F & -p & M_F \end{pmatrix} \\ & \quad \times \sum_{N_0} (-1)^{N_1+S-J_1+J_0+1+N_0+\Lambda_1-\bar{\Omega}} (2N_0+1) \begin{Bmatrix} N_1 & S & J_1 \\ J_0 & 1 & N_0 \end{Bmatrix} \begin{pmatrix} 1 & N_1 & N_0 \\ q & -\Lambda_1 & \Lambda_0 \end{pmatrix} \begin{pmatrix} S & J_0 & N_0 \\ \Sigma & -\bar{\Omega} & -\Lambda_0 \end{pmatrix} \\ & = (-1)^{F_0+F_1+J_0+2J_1+I-2\Lambda_1-M_F} \sqrt{(2F_0+1)(2F_1+1)(2J_0+1)(2J_1+1)(2N_1+1)} \\ & \quad \times \begin{Bmatrix} J_1 & F_1 & I \\ F_0 & J_0 & 1 \end{Bmatrix} \begin{pmatrix} F_1 & 1 & F_0 \\ -M_F & -p & M_F \end{pmatrix} \begin{pmatrix} N_1 & S & J_1 \\ -\Lambda_1 & \Sigma & -m \end{pmatrix} \begin{pmatrix} J_0 & 1 & J_1 \\ -\bar{\Omega} & q & m \end{pmatrix}, \end{aligned} \quad (\text{B7})$$

where $\langle j_1 || T^{(k)} || j_0 \rangle$ is the reduced matrix element. The first and the fifth equalities use the Wigner-Eckert theorem; the second and the fourth ones use the simplification of the spherical-tensor product; the third one uses the basis transformation of case (a) to case (b), given in Eq. (A9); the sixth one uses the equation $\langle N_1 || D^{(1)*} || N_0 \rangle = \sqrt{(2N_0+1)(2N_1+1)}$; and the seventh one uses the relation between the 3- j and 6- j symbols [2]. In this work, $p = 0$ is adapted because now we consider excitation with linearly polarized light. Then, we can obtain the coefficient as

$$C_{F_1}^{(F_0, M_F)} = A \times (-1)^{F_0+F_1-M_F} \sqrt{(2F_0+1)(2F_1+1)} \begin{Bmatrix} J_1 & F_1 & I \\ F_0 & J_0 & 1 \end{Bmatrix} \begin{pmatrix} F_1 & 1 & F_0 \\ -M_F & 0 & M_F \end{pmatrix}, \quad (\text{B8})$$

with

$$\begin{aligned} A & = N E_0^{(1)} \frac{\langle v_1 | v_0 \rangle}{\sqrt{2\hbar\Delta\omega}} \{1 - \varepsilon(-1)^{J_0+S+N_1+1}\} \sum_q \langle A^2 \Sigma^+ | \mu_q^{(1)} | X^2 \Pi \rangle (-1)^{J_0+J_1-N_1+I+2\bar{\Omega}-2\Lambda_1} \sqrt{(2J_0+1)(2J_1+1)(2N_1+1)} \\ & \quad \times \begin{pmatrix} N_1 & S & J_1 \\ \Lambda_1 & \Sigma & m \end{pmatrix} \begin{pmatrix} J_0 & 1 & J_1 \\ \bar{\Omega} & q & m \end{pmatrix}. \end{aligned} \quad (\text{B9})$$

Here, N is the normalization coefficient which makes the trace of the density matrix to be unity.

APPENDIX C: MOLECULAR-AXIS ANGULAR DISTRIBUTION OF THE STATE MULTIPOLE MOMENT

The molecular-axis angular distribution of the state multipole moment can be defined by the linear combination of those of $|J, M_J\rangle$ as

$$\begin{aligned} f_0^{(k)}(\theta) &\equiv \sum_{M_J} (-1)^{J-M_J} \langle JM_J, J - M_J | k0 \rangle f_{J, M_J}(\theta) \\ &= \sum_{M_J} (-1)^{J-M_J} \langle JM_J, J - M_J | k0 \rangle \sum_{M_S} \langle \theta | \langle SM_S | N \Lambda S J M_J \rangle \langle N \Lambda S J M_J | SM_S \rangle | \theta \rangle. \end{aligned} \quad (\text{C1})$$

The inner product of the state vector of Hund's case (b) and the space-fixed spin vector is described by using the state vector of Hund's case (a),

$$\langle SM_S | N \Lambda S J M_J \rangle = \sqrt{\frac{2N+1}{2J+1}} \sum_{\Omega, \Sigma} \langle N \Lambda, S \Sigma | J \Omega \rangle | J \Omega M_J \rangle D_{M_S \Sigma}^{(S)}, \quad (\text{C2})$$

where we use the transformation of case (b) to case (a) [66]

$$|N \Lambda S J M_J \rangle = \sqrt{\frac{2N+1}{2J+1}} \sum_{\Omega, \Sigma} \langle N \Lambda, S \Sigma | J \Omega \rangle | J \Omega M_J \rangle | S \Sigma \rangle = \sqrt{\frac{2N+1}{2J+1}} \sum_{\Omega, \Sigma, M'_S} \langle N \Lambda, S \Sigma | J \Omega \rangle | J \Omega M_J \rangle D_{M'_S \Sigma}^{(S)} | S M'_S \rangle, \quad (\text{C3})$$

and that of the space-fixed spin vector to the molecular-fixed one [66]:

$$|S \Sigma \rangle = \sum_{M_S} D_{M_S \Sigma}^{(S)} | S M_S \rangle. \quad (\text{C4})$$

Using Eqs. (C2) and (C3), we can obtain the relationship

$$\begin{aligned} \sum_{M_S} \langle SM_S | N \Lambda S J M_J \rangle \langle N \Lambda S J M_J | SM_S \rangle &= \frac{2N+1}{2J+1} \sum_{M_S} \sum_{\Omega, \Sigma} \langle N \Lambda, S \Sigma | J \Omega \rangle | J \Omega M_J \rangle D_{M_S \Sigma}^{(S)} \sum_{\Omega', \Sigma'} \langle N \Lambda, S \Sigma' | J \Omega' \rangle \langle J \Omega' M_J | D_{M_S \Sigma'}^{(S)*} \\ &= \frac{2N+1}{2J+1} \sum_{\Omega, \Sigma} \langle N \Lambda, S \Sigma | J \Omega \rangle | J \Omega M_J \rangle \sum_{\Omega', \Sigma'} \langle N \Lambda, S \Sigma' | J \Omega' \rangle \langle J \Omega' M_J | \delta_{\Sigma \Sigma'} \\ &= \frac{2N+1}{2J+1} \sum_{\Omega, \Sigma} \langle N \Lambda, S \Sigma | J \Omega \rangle^2 | J \Omega M_J \rangle \langle J \Omega M_J |. \end{aligned} \quad (\text{C5})$$

Thus, we can rewrite (C1) as

$$\begin{aligned} f_0^{(k)}(\theta) &= \frac{2J+1}{4\pi} \sum_{M_J} (-1)^{J-M_J} \langle JM_J, J - M_J | k0 \rangle \frac{2N+1}{2J+1} \sum_{\Omega, \Sigma} \langle N \Lambda, S \Sigma | J \Omega \rangle^2 \langle \theta | J \Omega M_J \rangle \langle J \Omega M_J | \theta \rangle \\ &= \frac{2N+1}{2J+1} \sum_{\Omega, \Sigma} \langle N \Lambda, S \Sigma | J \Omega \rangle^2 \sum_{M_J} (-1)^{J-M_J} \langle JM_J, J - M_J | k0 \rangle \langle \theta | J \Omega M_J \rangle \langle J \Omega M_J | \theta \rangle \\ &= \frac{2N+1}{2J+1} \sum_{\Omega, \Sigma} \langle N \Lambda, S \Sigma | J \Omega \rangle^2 \sum_{M_J} (-1)^{J-M_J} \langle JM_J, J - M_J | k0 \rangle (-1)^{M_J - \Omega} \sqrt{\frac{2J+1}{4\pi}} D_{-M_J - \Omega}^{(J)} \sqrt{\frac{2J+1}{4\pi}} D_{M_J \Omega}^{(J)} \\ &= \frac{2N+1}{4\pi} \sum_{\Omega, \Sigma} (-1)^{J-\Omega} \langle N \Lambda, S \Sigma | J \Omega \rangle^2 \sum_{M_J} \langle JM_J, J - M_J | k0 \rangle (-1)^{-M_J + \Omega} D_{-\Omega - M_J}^{(J)} (-1)^{M_J - \Omega} D_{\Omega M_J}^{(J)} \\ &= \frac{2N+1}{4\pi} \sum_{\Omega, \Sigma} (-1)^{J-\Omega} \langle N \Lambda, S \Sigma | J \Omega \rangle^2 \langle J \Omega, J - \Omega | k0 \rangle D_{00}^{(k)} \\ &= \frac{2N+1}{4\pi} \sum_{\Omega, \Sigma} (-1)^{J-\Omega} \langle N \Lambda, S \Sigma | J \Omega \rangle^2 \langle J \Omega, J - \Omega | k0 \rangle P_k(\cos \theta), \end{aligned} \quad (\text{C6})$$

where $P_k(\cos \theta)$ is a Legendre polynomial of rank k . The fifth equality uses the relationship of the sums of products of the D matrix [67].

APPENDIX D: RECONSTRUCTION OF THE DENSITY MATRIX FROM THE STATE MULTIPOLE MOMENTS AT $t = 0$

The total density matrix is retrieved from state multipole moments by using Eq. (20). We assume that the coefficient $C_{F_1}^{(F_0, M_F)}$ is set real and to be consistent to Eq. (2), (i.e.); its sign is positive or negative when $F_0 + F_1 - M_F - S$ is even or odd, respectively. For

$(F_0, M_F) = (3/2, \pm 3/2)$, the total density matrix is equal to the partial density matrix $\rho_{F_1, F_2}^{(3/2, \pm 3/2)}$. For $(F_0, M_F) = (1/2, \pm 1/2)$, the excitation to $F = 5/2$ is forbidden because of the selection rule $\Delta F = \pm 1$. Thus, for $(F_0, M_F) = (3/2, \pm 1/2)$, the total density matrix elements with $(F_1, F_2) = (1/2, 5/2)$, $(3/2, 5/2)$, and $(5/2, 5/2)$ are equal to the partial density matrix elements. Next, all of the coherences for $(F_0, M_F) = (1/2, \pm 1/2)$, $(3/2, \pm 1/2)$ are assumed to be same, and their value is set as x as in Eq. (D1). Then, the first term of Eq. (D1) can be transformed to Eq. (D2). The second and third term of (D1) are also rearranged in Eqs. (D3) and (D4). The relationships between the total and the partial matrix elements are given as Eqs. (D5)–(D7). Unknown 7 parameters ($x, \rho_{1/2, 1/2}^{(1/2, \pm 1/2)}, \rho_{3/2, 3/2}^{(1/2, \pm 1/2)}, \rho_{1/2, 3/2}^{(1/2, \pm 1/2)}, \rho_{1/2, 1/2}^{(3/2, \pm 1/2)}, \rho_{3/2, 3/2}^{(3/2, \pm 1/2)}, \rho_{1/2, 3/2}^{(3/2, \pm 1/2)}$) are determined by the seven simultaneous equations (D1)–(D7). Finally, $x = 0.89$ and all of the partial density matrix elements $\rho_{F_1, F_2}^{(F_0, M_F)}$ are reconstructed as shown in Table IV.

$$\frac{|\rho_{1/2, 3/2}^{(3/2, \pm 1/2)}|}{\sqrt{\rho_{1/2, 1/2}^{(3/2, \pm 1/2)} \rho_{3/2, 3/2}^{(3/2, \pm 1/2)}}} = \frac{|\rho_{1/2, 5/2}^{(3/2, \pm 1/2)}|}{\sqrt{\rho_{1/2, 1/2}^{(3/2, \pm 1/2)} \rho_{5/2, 5/2}^{(3/2, \pm 1/2)}}} = \frac{|\rho_{3/2, 5/2}^{(3/2, \pm 1/2)}|}{\sqrt{\rho_{3/2, 3/2}^{(3/2, \pm 1/2)} \rho_{5/2, 5/2}^{(3/2, \pm 1/2)}}} = \frac{|\rho_{1/2, 3/2}^{(1/2, \pm 1/2)}|}{\sqrt{\rho_{1/2, 1/2}^{(1/2, \pm 1/2)} \rho_{3/2, 3/2}^{(1/2, \pm 1/2)}}} = x, \quad (\text{D1})$$

$$\rho_{1/2, 3/2}^{(3/2, \pm 1/2)} = x C_{1/2}^{(3/2, \pm 1/2)} C_{3/2}^{(3/2, \pm 1/2)*} = x \frac{\rho_{1/2, 5/2}^{(3/2, \pm 1/2)} \rho_{3/2, 5/2}^{(3/2, \pm 1/2)}}{\rho_{5/2, 5/2}^{(3/2, \pm 1/2)}}, \quad (\text{D2})$$

$$\rho_{1/2, 1/2}^{(3/2, \pm 1/2)} = C_{1/2}^{(3/2, \pm 1/2)} C_{1/2}^{(3/2, \pm 1/2)*} = \frac{(\rho_{1/2, 5/2}^{(3/2, \pm 1/2)})^2}{x^2 \rho_{5/2, 5/2}^{(3/2, \pm 1/2)}}, \quad (\text{D3})$$

$$\rho_{3/2, 3/2}^{(3/2, \pm 1/2)} = C_{3/2}^{(3/2, \pm 1/2)} C_{3/2}^{(3/2, \pm 1/2)*} = \frac{(\rho_{3/2, 5/2}^{(3/2, \pm 1/2)})^2}{x^2 \rho_{5/2, 5/2}^{(3/2, \pm 1/2)}}, \quad (\text{D4})$$

$$\rho_{1/2, 1/2}^{(1/2, \pm 1/2)} = \rho_{1/2, \pm 1/2, 1/2, \pm 1/2} - \rho_{1/2, 1/2}^{(3/2, \pm 1/2)}, \quad (\text{D5})$$

$$\rho_{3/2, 3/2}^{(1/2, \pm 1/2)} = \rho_{3/2, \pm 1/2, 3/2, \pm 1/2} - \rho_{3/2, 3/2}^{(3/2, \pm 1/2)}, \quad (\text{D6})$$

$$\rho_{1/2, 3/2}^{(1/2, \pm 1/2)} = \rho_{1/2, \pm 1/2, 3/2, \pm 1/2} - \rho_{1/2, 3/2}^{(3/2, \pm 1/2)}. \quad (\text{D7})$$

-
- [1] U. Fano and J. H. Macek, *Rev. Mod. Phys.* **45**, 553 (1973).
[2] R. N. Zare, *Angular Momentum* (Wiley, New York, 1990), pp. 226–242.
[3] A. J. Orr-Ewing and R. N. Zare, *Annu. Rev. Phys. Chem.* **45**, 315 (1994).
[4] H. J. Andrä, *Phys. Rev. Lett.* **25**, 325 (1970).
[5] D. J. Lynch, C. W. Drake, M. J. Alguard, and C. E. Fairchild, *Phys. Rev. Lett.* **26**, 1211 (1971).
[6] D. J. Burns and W. H. Hancock, *Phys. Rev. Lett.* **27**, 370 (1971).
[7] H. G. Berry and J. L. Subtil, *Phys. Rev. Lett.* **27**, 1103 (1971).
[8] H. G. Berry, J. L. Subtil, E. H. Pinnington, H. J. Andrä, W. Wittmann, and A. Gaupp, *Phys. Rev. A* **7**, 1609 (1973).
[9] J. S. Deech, R. Luypaert, and G. W. Series, *J. Phys. B: At. Mol. Phys.* **8**, 1406 (1975).
[10] E. Hack and J. R. Huber, *Int. Rev. Phys. Chem.* **10**, 287 (1991).
[11] M. Dubs, J. Mühlbach, H. Bitto, P. Schmidt, and J. R. Huber, *J. Chem. Phys.* **83**, 3755 (1985).
[12] M. Dubs, P. Schmidt, and J. R. Huber, *J. Chem. Phys.* **85**, 6335 (1986).
[13] M. L. Costen, H. J. Crichton, and K. G. McKendrick, *J. Chem. Phys.* **120**, 7910 (2004).
[14] K. L. Reid, S. P. Duxon, and M. Towrie, *Chem. Phys. Lett.* **228**, 351 (1994).
[15] N. C.-M. Bartlett, D. J. Miller, R. N. Zare, A. J. Alexander, D. Sofikitis, and T. P. Rakitzis, *Phys. Chem. Chem. Phys.* **11**, 142 (2009).
[16] N. C.-M. Bartlett, J. Jankunas, R. N. Zare, and J. A. Harrison, *Phys. Chem. Chem. Phys.* **12**, 15689 (2010).
[17] D. Sofikitis, L. Rubio-Lago, M. R. Martin, D. J. A. Brown, N. C.-M. Bartlett, R. N. Zare, and T. P. Rakitzis, *J. Chem. Phys.* **127**, 144307 (2007).
[18] K. L. Reid, *Chem. Phys. Lett.* **215**, 25 (1993).
[19] M. Rukowski and H. Zacharias, *Chem. Phys.* **301**, 189 (2004).
[20] H. Stapelfeldt and T. Seideman, *Rev. Mod. Phys.* **75**, 543 (2003).
[21] Y. Ohshima and H. Hasegawa, *Int. Rev. Phys. Chem.* **29**, 619 (2010).
[22] C. P. Koch, M. Lemesko, and D. Sugny, *Rev. Mod. Phys.* **91**, 035005 (2019).
[23] K. Lin, I. Tutunnikov, J. Ma, J. Qiang, L. Zhou, O. Faucher, Y. Prior, I. Sh. Averbukh, and J. Wu, *Adv. Photonics* **2**, 024002 (2020).
[24] J. Küpper, S. Stern, L. Holmegaard, F. Filsinger, A. Rouzée, A. Rudenko, P. Johnsson, A. V. Martin, M. Adolph, A. Aquila, S. Bajt, A. Barty, C. Bostedt, J. Bozek, C. Caleman, R. Coffee, N. Coppola, T. Delmas, S. Epp, B. Erk *et al.*, *Phys. Rev. Lett.* **112**, 083002 (2014).
[25] J. Yang, J. Beck, C. J. Uiterwaal, and M. Centurion, *Nat. Commun.* **6**, 8172 (2015).
[26] B. L. Yoder, R. Bisson, and R. D. Beck, *Science* **329**, 553 (2010).

- [27] W. E. Perreault, N. Mukherjee, and R. N. Zare, *Science* **358**, 356 (2017).
- [28] C. Z. Bisgaard, O. J. Clarkin, G. Wu, A. M. D. Lee, O. Gessner, C. C. Hayden, and A. Stolow, *Science* **323**, 1464 (2009).
- [29] O. Schalk and A. E. Boguslavskiy, *J. Phys. Chem. A* **121**, 9612 (2017).
- [30] D. W. Chandler and P. L. Houston, *J. Chem. Phys.* **87**, 1445 (1987).
- [31] *Imaging in Molecular Dynamics: Technology and Applications*, edited by B. Whitaker (Cambridge University Press, Cambridge, 2003).
- [32] J. R. A. Heck and D. W. Chandler, *Annu. Rev. Phys. Chem.* **46**, 335 (1995).
- [33] M. N. R. Ashfold, N. H. Nahler, A. J. Orr-Ewing, O. P. J. Vieuxmaire, R. L. Toomes, T. N. Kitsopoulos, I. A. Garcia, D. A. Chestakov, S.-M. Wu, and D. H. Parker, *Phys. Chem. Chem. Phys.* **8**, 26 (2006).
- [34] A. Stolow, A. E. Bragg, and D. M. Neumark, *Chem. Rev.* **104**, 1719 (2004).
- [35] T. Suzuki, *Annu. Rev. Phys. Chem.* **57**, 555 (2006).
- [36] F. Rosca-Pruna and M. J. J. Vrakking, *Phys. Rev. Lett.* **87**, 153902 (2001).
- [37] F. Rosca-Pruna and M. J. J. Vrakking, *J. Chem. Phys.* **116**, 6567 (2002).
- [38] P. W. Dooley, I. V. Litvinyuk, K. F. Lee, D. M. Rayner, M. Spanner, D. M. Villeneuve, and P. B. Corkum, *Phys. Rev. A* **68**, 023406 (2003).
- [39] K. Mizuse, K. Kitano, H. Hasegawa, and Y. Ohshima, *Sci. Adv.* **1**, e1400185 (2015).
- [40] K. Lin, Q. Song, X. Gong, Q. Ji, H. Pan, J. Ding, H. Zeng, and J. Wu, *Phys. Rev. A* **92**, 013410 (2015).
- [41] E. T. Karamatskos, S. Raabe, T. Mullins, A. Trabattoni, P. Stammer, G. Goldsztejn, R. R. Johansen, K. Długołęcki, H. Stapelfeldt, M. J. J. Vrakking, S. Trippel, A. Rouzée, and J. Küpper, *Nat. Commun.* **10**, 3364 (2019).
- [42] R. A. Rose, A. J. Orr-Ewing, C.-H. Yang, K. Vidma, G. C. Groenenboom, and D. H. Parker, *J. Chem. Phys.* **130**, 034307 (2009).
- [43] K. Grygoryeva, J. Rakovský, O. Votava, and M. Fárník, *J. Chem. Phys.* **147**, 013901 (2017).
- [44] E. F. Thomas, A. A. Søndergaard, B. Shepperson, N. E. Henriksen, and H. Stapelfeldt, *Phys. Rev. Lett.* **120**, 163202 (2018).
- [45] K. Sonoda, S. Fukahori, and H. Hasegawa, *Phys. Rev. A* **103**, 033118 (2021).
- [46] K. Mizuse, R. Fujimoto, N. Mizutani, and Y. Ohshima, *JoVE* **120**, e54917 (2017).
- [47] K. Mizuse, R. Fujimoto, and Y. Ohshima, *Rev. Sci. Instrum.* **90**, 103107 (2019).
- [48] K. Mizuse, N. Sakamoto, R. Fujimoto, and Y. Ohshima, *Phys. Chem. Chem. Phys.* **22**, 10853 (2020).
- [49] K. Ueno, K. Mizuse, and Y. Ohshima, *Phys. Rev. A* **103**, 053104 (2021).
- [50] J. A. Gray, R. L. Farrow, J. L. Durant, and L. R. Thorne, *J. Chem. Phys.* **99**, 4327 (1993).
- [51] M. Brouard, H. Chadwick, Y.-P. Chang, B. J. Howard, S. Marinakis, N. Screen, S. A. Seamons, and A. L. Via, *J. Mol. Spectrosc.* **282**, 42 (2012).
- [52] R. J. Miller, W. L. Glab, and B. A. Bushaw, *J. Chem. Phys.* **91**, 3277 (1989).
- [53] T. Bergeman and R. N. Zare, *J. Chem. Phys.* **61**, 4500 (1974).
- [54] J. J. Gallagher, F. D. Bedard, and C. M. Johnson, *Phys. Rev.* **93**, 729 (1954).
- [55] E. M. Weinstock, R. N. Zare, and L. A. Melton, *J. Chem. Phys.* **56**, 3456 (1972).
- [56] A. Timmermann and R. Wallenstein, *Opt. Commun.* **39**, 239 (1981).
- [57] T. Endo, A. Matsuda, M. Fushitani, T. Yasuike, O. I. Tolstikhin, T. Morishita, and A. Hishikawa, *Phys. Rev. Lett.* **116**, 163002 (2016).
- [58] T. Endo, H. Fujise, H. Hasegawa, A. Matsuda, M. Fushitani, O. I. Tolstikhin, T. Morishita, and A. Hishikawa, *Phys. Rev. A* **100**, 053422 (2019).
- [59] K. Nakamura, S. Fukahori, and H. Hasegawa, *J. Chem. Phys.* **155**, 174308 (2021).
- [60] K. Mizuse, N. Chizuwa, D. Ikeda, T. Imajo, and Y. Ohshima, *Phys. Chem. Chem. Phys.* **20**, 3303 (2018).
- [61] J. J. Gallagher and C. M. Johnson, *Phys. Rev.* **103**, 1727 (1956).
- [62] A. Omont, *Prog. Quantum Electron.* **5**, 69 (1977).
- [63] J. Luque and D. R. Crosley, *J. Chem. Phys.* **111**, 7405 (1999).
- [64] J. Luque and D. R. Crosley, *J. Chem. Phys.* **112**, 9411 (2000).
- [65] T. B. Settersten, B. D. Patterson, and W. H. Humphries IV, *J. Chem. Phys.* **131**, 104309 (2009).
- [66] T. Tanaka, *Formula of Angular Momentum: Part 1* (Japan Society for Molecular Science, Tokyo, 2007), 1st ed., AC0001, in Japanese, www.j-molsci.jp/archives/AC0001.pdf.
- [67] D. A. Varshalovich, A. N. Moskalev, and V. K. Khersonskii, *Quantum Theory of Angular Momentum* (World Scientific, Singapore, 1988), p. 85.